Satellite hole formation during dewetting: experiment and simulation

2003 J. Phys.: Condens. Matter 15 3355

(http://iopscience.iop.org/0953-8984/15/19/334)

INSTITUTE OF PHYSICS PUBLISHING JOURNAL OF PHYSICS: CONDENSED MATTER

J. Phys.: Condens. Matter **15** (2003) 3355–3366 PII: S0953-8984(03)55043-3

Satellite hole formation during dewetting: experiment and simulation

Chiara Neto[1,4], Karin Jacobs[1,4,5], Ralf Seemann[1], Ralf Blossey[2], Jürgen Becker[3] and Günther Grün[3]

[1] Department of Applied Physics, University of Ulm, Albert Einstein Allee 11, D-89069 Ulm, Germany
[2] Centre for Bioinformatics, Saarland University, PO Box 151150, D-66041 Saarbrücken, Germany
[3] Institute of Applied Mathematics, University of Bonn, Beringstraße 6, D-53115 Bonn, Germany

E-mail: k.jacobs@physik.uni-saarland.de

Received 22 October 2002
Published 6 May 2003
Online at stacks.iop.org/JPhysCM/15/3355

Abstract

The dewetting of thin polymer films on solid substrates has been studied extensively in recent years. These films can decay either by nucleation events or by spinodal dewetting, essentially only depending on the interface potential describing the short- and long-range intermolecular interactions between the interfaces and the initial film thickness. Here, we describe experiments and simulations concerned with the decay of polystyrene thin films. The rupture of the film occurs by the formation of a correlated pattern of holes ('satellite holes') along the liquid rims accumulating at the channel borders. The development of this complex film rupture process, which is neither simply spinodal nor nucleation dewetting, can be mimicked precisely by making use of a novel simulation code based on a rigorous mathematical treatment of the thin film equation and on the knowledge of the effective interface potential of the system. The conditions that determine the appearance and the position of the satellite holes around pre-existing holes are discussed.

(Some figures in this article are in colour only in the electronic version)

1. Introduction

The spreading of a liquid on a solid surface and the stability of the resulting film are issues of major importance not only in a number of technological applications, such as paints, surface coatings, lubrication and textile dyeing, but also in fundamental studies of surface physics. The thermodynamic stability and the dynamics of thin films on solid surfaces have been addressed in numerous studies, both experimental and theoretical [1–5]. Much of this work

[4] Present address: Experimental Physics, Saarland University, PO Box 151150, D-66041 Saarbrücken, Germany.
[5] Author to whom any correspondence should be addressed.

has involved polymer films, both because of their technological relevance and because the high viscosity of polymers makes the experimental timescales practical to work with [6–12].

If a liquid wets a surface completely, it will spontaneously form a continuous and uniform film on top of it. Liquids that do not wet a surface can be forced to form uniform films on the substrates by techniques such as spin coating, dip coating or spraying. However, in this case the films are generally not stable. If allowed to reach thermodynamic equilibrium (e.g. if heated above the glass transition temperature), the films will transform, via a symmetry-breaking process named 'dewetting', into their equilibrium state, i.e. a series of isolated droplets with a finite contact angle given by Young's equation [13].

The rupture mechanisms in thin films (thickness $<$100 nm) are mainly of two types [14, 15]. The first is thermal nucleation, giving rise to the formation of uncorrelated holes in a metastable film. In polymer films, thermal nucleation is seldom a purely homogeneous event but rather heterogeneous since the presence of debris particles or impurities in the film lowers the thermal energy barrier [16, 17].

The second is a spontaneous rupture process occurring when thermal fluctuations induce surface undulations in an unstable film. These fluctuations in film thickness grow with time, leading to holes as soon as the amplitude of the fluctuations reaches the value of the film thickness [18, 19]. This mechanism is called spinodal dewetting, in analogy to the decomposition that takes place in a mixture of immiscible liquids [20, 21], and has been studied in detail more recently [7, 15, 22, 23].

In consequence of the hole formation process, the removed material accumulates at the boundary of the holes, forming a rim. The width and the height of the rim and the diameter of the hole grow with time [13, 16, 17, 24] until the hole impinges on adjacent holes, resulting in the formation of ribbons of liquid along their contact line. Finally, the ribbons are transformed into droplets by a Rayleigh instability.

In the present work we focus on dewetting of very thin, low molecular weight polystyrene (PS) films of thickness between 4 and 30 nm. In some experiments, dewetting was artificially triggered by scratching an initially uniform film, resulting in dry channels in the film (this process is hereafter referred to as indentation) [25]. We provide a direct comparison between experimental results, obtained by atomic force microscopy (AFM), and numerical results, obtained from simulations based on the lubrication equation. The simulations employ experimentally obtained data, namely the film thickness, the effective interface potential of the system [23] and the viscosity of thin PS films [26]. Results of experiments and simulations are in good agreement, in respect both to the particular patterns developed upon dewetting and to their temporal evolution. The appearance of so-called 'satellite holes' is shown here to be not a special characteristic of volatile liquids, as suggested by Kargupta *et al* [27], but a generic phenomenon in the dewetting of thin films, as recently reported by Becker *et al* [28]. The artificial indentations provide a direct and easy means to study the connection between local curvature of the hole rims and the appearance of satellite holes. On the basis of experiment and simulation we elucidate the mechanisms involved in the formation of the satellite holes.

2. Experimental details

Thin PS films were prepared using atactic PS with low molecular weight (PS 2.05 k: $M_w = 2.05$ kg mol^{-1}, $M_w/M_n = 1.05$; Polymer Labs, Church Stretton, UK; radius of gyration $R_g = 1.4$ nm). The polymer is non-volatile, i.e. the film mass is conserved. Given the relatively low molecular weight of the PS (about 20 monomers/molecule), it can be treated in a first approach as a Newtonian fluid in its melt state and therefore viscoelastic effects are ignored in the simulations. Thin films were prepared by spin casting dilute toluene solutions (Selectipur

toluene, Merck, Germany) of PS on polished oxidized silicon wafers (Silchem GmbH, Freiberg, Germany). The silicon wafers (Si) are covered with a layer of amorphous silicon oxide of thickness 192 ± 1 nm. Prior to spin coating, the silicon wafers were very thoroughly cleaned in order to eliminate organic and particulate contaminants. Debris particles were eliminated using a CO_2-snow jet [29]. Subsequently, the wafers were treated with ultrasound for a few minutes in ethanol, acetone and toluene and immersed in fresh piranha solution[6] (1:1 mixture of concentrated sulphuric acid and 30% H_2O_2) for 30 min and then thoroughly rinsed with hot Milli-Q water. Cleaning and spin coating were performed in a class-100 laminar flow cabinet. The prepared films were kept in a laminar flow cabinet at room temperature for at least 10 h prior to measurements, in order to eliminate the possible presence of residual solvent.

The thicknesses of the silicon oxide layer (henceforth abbreviated SiO) and of the PS films were determined by ellipsometry (Multiscope by Optrel GdBR, Berlin, Germany), at different angles of incidence. The film thickness was derived from the measurements using the literature value for the refractive index of PS ($n = 1.59$, [30]). The literature value of n was tested in measurements performed on thicker PS films and was found to coincide with the measured one within the experimental error. The prepared PS films (of thickness between about 4 and 30 nm) were smooth and uniform, with an RMS roughness below 0.3 nm (over an area of 1000×1000 nm^2) as determined by AFM (Nanoscope III, Digital Instruments, Santa Barbara). The RMS roughness of a clean silicon wafer over the same area was lower than 0.2 nm. The polymer films were characterized via ellipsometry and AFM within a few days of preparation. Since PS films up to a thickness of approximately 300 nm are unstable on these substrates [23, 31], thermal annealing induced dewetting of the spin-cast films. Annealing was performed *in situ* under the atomic force microscope head in order to follow the dewetting process in real time. Sample temperatures between 50 and 60 °C could be maintained constant within 0.1 °C using the Digital Instruments heating stage and controller (model HS-1).

The prepared films were observed both as-prepared and after dry channels were indented in them. The channels were indented on the PS films at about 35 °C, i.e. above the glass transition temperature of such thin polymer films [26], but at temperatures where the dewetting process is still very slow. Both the indenting process and the imaging of the dewetting patterns were performed via AFM operating in tapping mode™. For the indentation, a silicon AFM tip (force constant 42 N m^{-1}, Nanosensors GmbH, Germany) was brought into hard contact with the polymer film and was driven across the film for the length of a few micrometres. As a result, material was removed from the substrate and indentations of controlled morphology were formed on the films.

In particular, linear channels and intersections between two linear channels were created. In figures 1(a)–(c) we show examples of various indentations performed on different PS films with AFM tips using the procedure described above. Figures 1(b) and (c) show two linear indentations forming an angle of approximately 45° and 90°, respectively. Indented channels were on average around 600 nm in width when first formed and approximately as deep as the polymer film thickness.

Within a few minutes after the indentation, a new AFM tip was mounted in the AFM tip-holder and the samples were scanned continuously while being heated at the chosen annealing temperature (53°–56°C). Low tapping forces and relatively low scan rates were employed in order not to affect the liquid layer with the scanning motion [31]. The experiments are compared with simulations employing as initial data similar geometries to the ones used in the experiments. We start with a step in a film of thickness 4.4 nm (see figure 2(i)) and a wedge of polymer of the same thickness (see figure 3(g)). Note that the bottom of the dewetted

[6] Caution: piranha solution may explode upon contact with organic solvents.

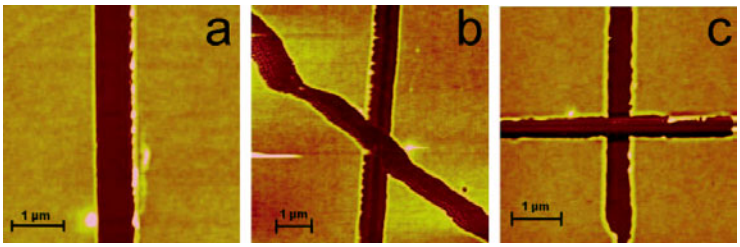

Figure 1. AFM images of different indentation geometries formed by pressing AFM tips on thin (<7 nm) PS (2.05 k) films. The height scale is 18 nm for all images.

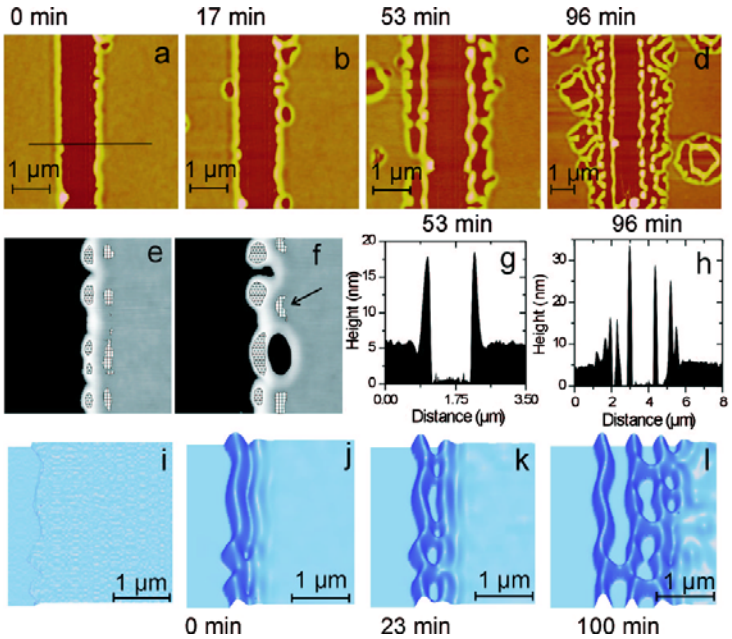

Figure 2. Testing a linear geometry. (a)–(d) AFM images of a 5.6 ± 0.5 nm PS (2.05 k) film dewetting on a Si/SiO wafer. (e) is a magnification of a threshold image recorded 7 min before the image in (a). (f) is a magnification of the threshold image of (b) (see text). (g) and (h) show cross sections of AFM scans taken at the position of the line in image (a). (i)–(l) Simulation results for a 4.4 nm PS film dewetting on a Si/SiO wafer. Simulations were performed assuming a polymer film viscosity of 12 000 Pa s [26]. (i) represents the starting geometry of the simulation. The height scale varies from 35 nm in (a), to 40 nm in (b) and to 55 nm in (c) and (d).

areas is not coincident with the SiO. As previously reported, the bottom of a hole in PS films dewetting on these substrates is not 'dry', but is still covered with a residual wetting film of PS having an equilibrium film thickness of approximately 1.3 nm [23]. In our experiments we also found evidence for the existence of a wetting layer.

3. Concepts of modelling and simulation

The disparity between vertical and horizontal length scales, as well as the observation that contact angles exceeding $\frac{\pi}{2}$ do not occur, admit the use of the lubrication approximation to

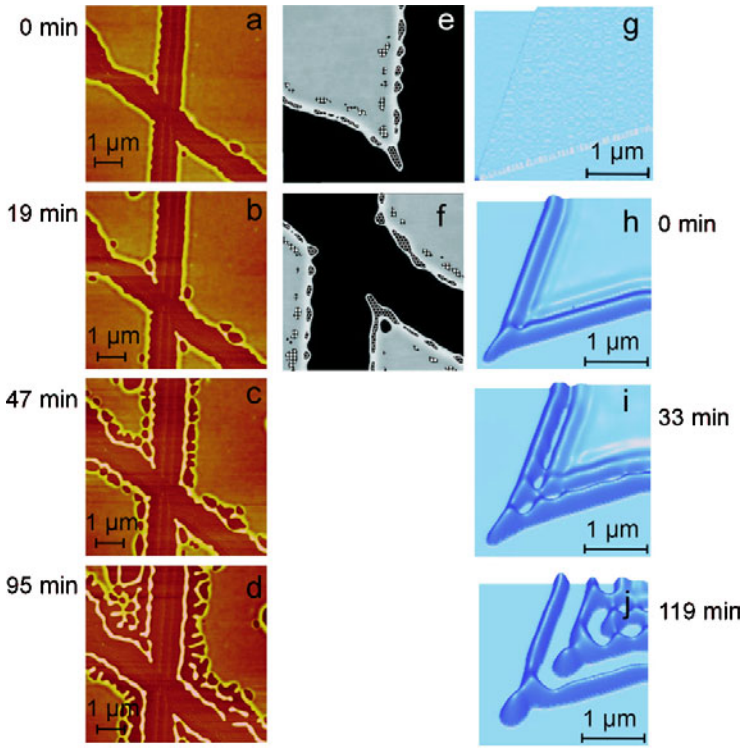

Figure 3. Testing a wedge geometry. (a)–(d) AFM images and (g)–(j) simulations are compared for a 4.4 nm PS film dewetting on an Si/SiO wafer. Simulations refer to a polymer film viscosity of 12 000 Pa s [26]. (g) represents the starting geometry of the simulation. The height scale is 38 nm in (a)–(d). (e) is a magnification of a threshold image recorded 10 min before the image in (a). (f) is a magnification of a threshold image of (a) (see text).

describe the film evolution. Assuming the free energy to be given by

$$\int_\Omega \frac{\sigma}{2}|\nabla u|^2 + W(u), \tag{1}$$

where u is the thickness of the liquid film, σ is the surface tension and $W(u)$ is the effective interface potential, and supposing that energy is solely dissipated due to viscous friction, we arrive at the thin film equation

$$\eta u_t - \operatorname{div}(m(u)\nabla p) = 0, \tag{2}$$

where η is the viscosity and where $m(u)$ is a non-negative mobility coefficient and is given by $m(u) = \frac{1}{3}u^3$ for a no-slip boundary condition at the solid–liquid interface. The generalized Laplace pressure p is given by

$$p = -\sigma\,\Delta u + W'(u). \tag{3}$$

The effective interface potential for the experimental system under consideration can be written as

$$W(u) = \frac{c}{u^8} - \frac{A_{\mathrm{SiO}}}{12\pi u^2}, \tag{4}$$

where c denotes the strength of the short-range part of the potential, $c = 6.3(1) \times 10^{-76}$ J m^6, and A_{SiO} is the Hamaker constant of PS on SiO, $A_{\mathrm{SiO}} = 2.2(4) \times 10^{-20}$ J [23]. The global

minimum in $W(u)$ is at $u = 1.3 \pm 0.1$ nm, reflecting the equilibrium thickness of a PS film on an SiO wafer. For numerical purposes it is important to distinguish between stabilizing and destabilizing terms. Therefore, we decompose

$$W(u) = W_+(u) + W_-(u), \tag{5}$$

where the stabilizing term W_+ and the destabilizing term W_- are given by cu^{-8} and $-\frac{A_{\mathrm{SiO}}}{12\pi}u^{-2}$, respectively.

In general, smooth solutions of system (2), (3) are not expected to exist. Instead, we are looking for so-called *weak solutions* u, p that satisfy

$$\int_0^T \int_\Omega \eta u_t \phi + \int_0^T \int_\Omega m(u)\nabla p \nabla \phi = 0 \tag{6}$$

$$\int_0^T \int_\Omega p\psi = \int_0^T \int_\Omega \sigma \nabla u \nabla \psi + \int_0^T \int_\Omega W'(u)\psi \tag{7}$$

for all $\psi, \phi \in C^1((0,T)\times\Omega)$. Note that smooth solutions are also weak solutions. Moreover, the system (6), (7) is the starting point to develop finite element schemes (cf [32]).

Let us give the main ideas of the scheme. First, we have to introduce some notation. Let $\mathcal{T}_h$ be a regular and admissible triangulation of the spatial domain Ω (cf Ciarlet's monograph [33]) with simplicial elements, where the index h denotes the maximum diameter of a triangle $T \in \mathcal{T}_h$. Let us suppose in addition that the discretization is *rectangular*, in the sense that each triangle $T \in \mathcal{T}_h$ is a right-angled one. Note that this does not exclude the applicability of standard strategies for local mesh refinement. However, it places a slight restriction on the class of domains that can be considered.

By V^h, we denote the subspace of $H^{1,2}(\Omega)$ consisting of continuous functions which are linear on each triangle $T \in \mathcal{T}_h$. In the following, elements of V^h will be denoted by upper-case characters, functions contained in non-discrete function spaces will be denoted by lower-case characters. A function $V \in V^h$ is uniquely defined by its values on the set of nodes $\mathcal{N}_h = \{x_j\}_{j\in J}$ of the triangulation $\mathcal{T}_h$, where J denotes a corresponding index set. A set of basis functions dual to the set of nodal points $\mathcal{N}_h$ is given by the 'hat'-type functions $\phi_j \in V^h$ with $\phi_j(x_i) = \delta_{ij}$. Let us furthermore introduce the well-known lumped masses scalar product corresponding to the integration formula

$$(\Theta, \Psi)_h := \int_\Omega \mathcal{I}_h(\Theta\Psi) \tag{8}$$

where $\mathcal{I}_h : C^0(\Omega) \to V^h$ is the interpolation operator with $\mathcal{I}_h u = \sum_{j\in J} u(x_j)\phi_j$. By (u, v), we denote the usual L^2 scalar product on Ω.

Finally, let the time interval $I := [0, T]$ be subdivided into intervals $I_k = [t_k, t_{k+1})$ with $t_{k+1} = t_k + \tau_k$ for time increments $\tau_k > 0$ and $k = 0, \ldots, N-1$. Then, an implicit, backward Euler discretization scheme for the system (6), (7) reads as follows (see [34] and [35]):

For given $U^0 \in V^h$, *find a sequence* $(U^k, P^k) \in V^h \times V^h$, $k = 0, \ldots, N-1$ *such that*

$$\frac{\eta}{\tau_k}(U^{k+1} - U^k, \Phi)_h + (M(U^{k+1})\nabla P^{k+1}, \nabla\Phi) = 0 \tag{9}$$

$$(P^{k+1}, \Psi)_h = \sigma(\nabla U^{k+1}, \nabla\Psi) + (W'_+(U^{k+1}) + W'_-(U^k), \Psi)_h \tag{10}$$

for all $\Psi, \Phi \in V^h$.

For the discrete solutions U^k corresponding to the time steps $\{t_k\}_{k=1,\ldots,N}$ we then define a piecewise constant extension $U_{\tau h}$ by setting $U_{\tau h} = U^k$ for $t \in I_k$. A discrete pressure $P_{\tau h}$ can be defined by analogy.

Note that the destabilizing term W'_- is discretized explicitly, whereas the stabilizing term W'_+ is discretized implicitly. This distinction is essential to bound the free energy at arbitrary times $t > 0$ by the free energy of the initial data.

To obtain results on the convergence and positivity of discrete solutions the choice of the discrete version M of the mobility m is crucial. For example, if we simply defined $M(U)$ on each triangle T as the mean value of $m(U)$ on T, we could not expect discrete solutions to stay positive. Instead, we take $M(U)$ to be matrix valued: on a non-degenerate reference triangle $\hat{T}_{(\alpha_1,\alpha_2)} = co(0, \alpha_1 e_1, \alpha_2 e_2)$, where e_1, e_2 denotes the canonical basis of $\mathbb{R}^2$, we set (recall, that $m(u) = \frac{1}{3}u^3$)

$$\hat{M}(U) = \begin{pmatrix} \hat{M}_1 & 0 \\ 0 & \hat{M}_2 \end{pmatrix}, \tag{11}$$

with

$$\hat{M}_i = \left(\fint_{U(0)}^{U(\alpha_i e_i)} \frac{1}{m_\epsilon(s)} \, \mathrm{d}s \right)^{-1} \tag{12}$$

and $m_\epsilon := m(\max(\epsilon, u))$. Note, that for $U(\alpha_i e_i) = U(0)$ the definition simplifies to $\hat{M}_i = m(U(0))$. Because we use a rectangular discretization, each triangle $T \in \mathcal{T}_h$ can be mapped by an orthogonally affine equivalent transformation $x \mapsto \hat{x} = x_0 + A^{-1}x$, where A is an orthogonal matrix, onto a reference triangle $\hat{T}_{(\alpha_1,\alpha_2)}$. For such T, the mobility matrix is given by $M := A\hat{M}A^{-1}$ (for details, cf [32]).

This construction allows us to prove the existence of positive discrete solutions if initial data satisfy $U^0 \geqslant \varepsilon > 0$. Moreover the solution $U_{\tau h}$ satisfies the energy estimate, which reads as follows:

$$\begin{aligned} \eta\left(\int_\Omega \frac{\sigma}{2} |\nabla U^N(x)|^2 + \mathcal{I}_h W(U^N) \, \mathrm{d}x \right) + \int_0^T (M(U_{\tau h}) \nabla P_{\tau h}, \nabla P_{\tau h}) \, \mathrm{d}t \\ \leqslant \eta\left(\int_\Omega \frac{\sigma}{2} |\nabla U^0(x)|^2 + \mathcal{I}_h W(U^0) \, \mathrm{d}x \right). \end{aligned} \tag{13}$$

It can be obtained by choosing $\Phi = P^{k+1}$ in (9) and summing over k. Furthermore, if we define a (mathematical) entropy G by $G(s) = \int_A^s g(r) \, \mathrm{d}r$ and $g(s) = \int_A^s m_\epsilon(r)^{-1} \, \mathrm{d}r$ we are able to obtain the following entropy estimate by setting $\Phi = \mathcal{I}_h G'(U^{k+1})$ in (9) and summing over k:

$$\eta \int_\Omega \mathcal{I}_h G(U^N(x)) \, \mathrm{d}x + \sigma \int_{t_1}^T (\Delta_h U_{\tau h}, \Delta_h U_{\tau h})_h \, \mathrm{d}t \leqslant \eta \int_\Omega \mathcal{I}_h G(U^0(x)) \, \mathrm{d}x + R. \tag{14}$$

Here, R is a uniformly bounded quantity and Δ_h denotes the discrete Laplacian. Combining these estimates it can be shown that $U_{\tau h}$ converges strongly with respect to the topology of the Lebesgue–Sobolev space $L^2((0, T), H^{1,2}(\Omega))$ to a solution of the continuous problem as $\tau, h \to 0$ [35].

For the simulations presented in this paper, we used a version of the algorithm described above that is adaptive both in time and space. The time increment is chosen to be proportional to the ratio of grid size and the spatial maximum of the vertically averaged velocity of the horizontal flow, the latter being of the same order as $|M(U)\nabla P|/U$. The refinement of the spatial grid is controlled via the difference between spatial gradients on neighbouring triangles. Thus, we guarantee a precise resolution of the moving contact line (see [32] for experiments on the order of convergence).

4. Results and discussion

Figure 2 illustrates the temporal evolution of the indentation shown in figure 1(a). The dewetting experiment was carried out *in situ* on a PS film of thickness 5.6 ± 0.5 nm at an annealing temperature of 55 °C. The AFM image presented in figure 2(a) was captured 40 min after the one in figure 1(a) and 22 min after the temperature of 55 °C was reached. This image, in which the first satellite hole appears in the scanning area, is chosen as the origin of time for the experiment, $t_{sat} = 0$. Time indications given in the figures and in the remainder of the paper are calculated from this origin. Figures 2(b)–(d) show approximately the same region of the channel in subsequent stages of the dewetting process. As can be seen in the series of AFM images, some of the material artificially removed from the linear channel is accumulated in the two rims along the sides of the channel.

Typically, the scratching process was not symmetrical and more material was accumulated on one of the two rims. For example, in figure 1(a) the right side of the channel is higher and thicker than the left one, probably due to the tip geometry. As soon as the annealing temperature of 55 °C is reached, the channel undergoes a morphological modification. In particular, the channel width starts to increase from a value of 650 ± 20 nm, corresponding to figure 1(a), to 1040 ± 30 nm in figure 2(b). The moving rims grow in width and height, in consequence of the increasing volume of the polymer removed from the dewetted area, as can also be seen in the cross sections recorded at later times in figures 2(g)–(h). These cross sections of AFM scans were taken at the position indicated by the line in figure 2(a). Note that the height scale is greatly magnified compared to the lateral dimensions. On the inner side of the rim, at the three-phase contact line, in the following called the 'dry' side, the rim shape is determined by the receding contact angle of the polymer on the surface, in our case below 10°. On the outer side of the rim, the 'wet' side, the crest of material merges with the still uniform polymer film. We observe an undulatory behaviour of the rim profile in the direction perpendicular to the rim (figures 2(a)–(d)). In figures 2(a)–(d) and in the cross sections 2(g)–(h) it can be seen that the rim decreases to the thickness of the unperturbed film via a trough. This trough becomes deeper with time, until it eventually reaches the substrate and a hole is formed next to the rim.

From a theoretical point of view, the presence of the trough on the wet side of the rim is well understood [24, 36]. A simple qualitative explanation for the presence of the trough is given in the following. Initially, the surface of the film on the wet side of the rim has a negative curvature. This leads to flow from the rim and from the film towards this region. For mass conservation, small thickness fluctuations arise on the film surface next to this region. As soon as a small ditch has developed, the dewetting forces lead to a further deepening of the ditch, and eventually a hole is formed. Recent studies showed that a trough on the wet side of the rim could be observed on polymer films as thick as 60 nm, if the polymer melt was below the entanglement length [24, 36]. There it was shown that a disturbance in a film of Newtonian liquid should always decay via an undulation, as is evident from the fact that the Green function of the linearized lubrication equation always has an undulatory profile. Our experiments performed with a low molecular weight polymer confirm this finding. Viscoelastic properties of the liquid may alter this behaviour in so far as that for higher molecular weight polymers the characteristic trough on the wet side of the rim is completely suppressed.

These findings are also confirmed by the present simulation results, where no viscoelastic effects are taken into account (figures 2 (i)–(l)). The trough extends along the full length of the channel and holes appear in fast succession along the borders of the channel until a first row of holes frames the whole length of the channel. Then a second trough develops outside the first row of holes and further evolves into a row of holes, followed by a third and so on (figures 2 (d) and (l)). We call this type of cascade pattern 'satellite holes' [28, 36]. As observed in

simulations by Kargupta *et al* [27] for volatile thin films, the film could in principle still dewet spinodally, but the growth rate of the wavelength-correlated holes is slower and therefore dewetting by nucleation dominates.

The images presented in figure 2 help to answer a fundamental question regarding satellite holes, i.e. where satellite holes appear first and why. Figures 2(e) and (f) present two digitized AFM images, where the deeper parts of the trough have been highlighted with a square pattern and the highest parts of the rim have been highlighted with a triangle pattern. These images were obtained by imposing two height thresholds on the original AFM images, in order to display the very small height differences (about 1 nm) within the image. In the initial stage of dewetting, the borders of the channel are still approximately straight (as in figure 2(e)). At this stage, the locations at which the rim is higher correspond to locations at which the trough is deeper and the latter locations correspond directly to regions where satellite holes will appear first. Later on, when dewetting has progressed, the borders of the channels become more undulated (as in figure 2(f)) and the local in-plane curvature of the rim becomes important in determining the deepest sites of the trough. Indeed, when the rim is curved, the proximity of multiple regions of negative curvature enhances the deepening of the trough in the central region. In particular, in figure 2(f) the deepest site of the trough (indicated by the arrow) is situated between the rim of the first satellite hole and the rim of the channel. This region, where a wedge of polymer is bordered by rims, becomes the preferential site for the appearance of satellite holes. The simulation results confirm the experimental finding: as seen in figure 2(j), the first satellite holes appear in regions of the highest in-plane curvature of the rim.

All these elements suggest that the occurrence of satellite holes depends directly on the local difference in generalized Laplace pressure between the rim and the region on the wet side of the rim; where this difference is greater, the flow from the rim to this region will be faster and the ditch will appear first. Guided by this idea and in order to directly observe dewetting in a wedge geometry, we performed further experiments on films which were indented with cross geometries.

In figures 3(a)–(d), we present the temporal evolution of two indentations at an angle of 45°, which create two wedges of polymer film of approximately 45° and two of approximately 135°. The experiment was carried out *in situ* on a PS film of thickness 4.4 ± 0.5 nm at the annealing temperature of 54 °C. Figure 3(a) corresponds to $t_{sat} = 0$ and figures 3(b)–(d) show the same region of the indentations at successive times. Here too, after about 20 min from first reaching the annealing temperature, small holes start appearing along the rims of the channels. The threshold images in 3(e)–(f) show that the deepest sites of the trough (square pattern) are situated directly next to the highest sites of the rims (triangle pattern) and in particular at the apex of the wedges. As expected, the satellite holes appear first at the two acute wedge sites, then at the obtuse wedge sites and finally everywhere along the channel, next to the parts of the rims which are thicker.

The same effect is also very pronounced in the simulations: in figure 3(h), the first satellite hole appears at the intersection of the two rims, with the cascade progressing along the channels. At this stage we are not able to provide quantitative details of the rupture processes because, due to the presence of the artificial indentations, the evolution of the dewetting patterns cannot be described by linear stability analysis, as in the case of the spinodal dewetting scenario. A more detailed analysis of local curvature and flow velocities is in progress and will be presented in a future study.

In all the performed experiments, satellite holes appear initially along the channels and slightly later in the rest of the film. An example of this can be seen in figure 4, where the late stages of dewetting of the indentation geometries of figure 1 are shown. In figure 4(a) the initially indented cross is still visible, even if the arms of the cross have started to decay into

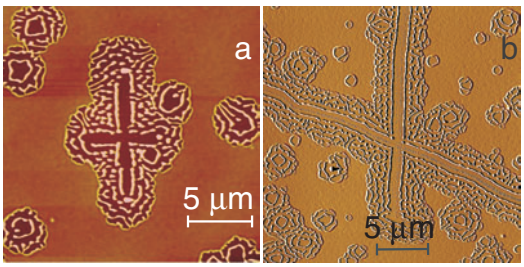

Figure 4. AFM images of PS films at a late stage of dewetting. (a) PS film 5.0±0.3 nm thick. (b) Shaded height image of a PS film 4.8 ± 0.4 nm thick. The height scale is 30 nm.

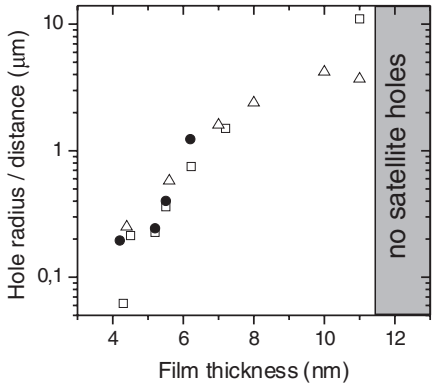

Figure 5. Summary of experiments and simulations performed on thin PS (2.05 k) films. The highest values of the radius of holes that did not show satellite holes in experiments are plotted as empty squares. Filled circles indicate the lowest value of the radius of each hole that showed satellite holes ($r_{unstable}$, see text) in experiments. Empty triangles indicate the distance covered by the straight front in simulations at the moment when satellite holes appeared. No satellite holes were observed in experiments or simulations in films of thickness greater than 11.5 ± 0.5 nm (shaded area). The error bars are approximately the size of the symbols.

shorter cylinders and droplets. At the top and at the bottom of the cross, four or five successive rims or lines of droplets can be seen, the remains of several rows of satellite holes around the initial channels. The round cascades present in the rest of the film (where no indentation was performed) have almost the same number of concentric rims, two or three. This effect is visible also in figure 4(b).

While the indentations are useful in order to study the effect of local curvature on the deepening of the trough, they also introduce additional perturbations in the experiments, which are difficult to account for in simulations. Therefore, we also performed experiments on non-indented films, which are more correctly compared with simulations in respect to hole-break-up times (or distances). These experiments led to the conclusion that the appearance of satellite holes is strongly dependent on the initial film thickness. Figure 5 presents a summary of results of experiments and simulations (the latter performed on a straight-front geometry). In experiments, we observed the spontaneous rupture of a nucleated central hole and the formation of round cascades around it (as in the outer portions of figure 4). The maximum radius of a central hole that did not present satellite holes is plotted in figure 5 as empty squares. For films of thickness between 4 and 7 nm, troughs were unstable and led to satellite holes only for hole radii greater than $r_{unstable}$ (plotted in figure 5 as filled circles). Figure 5 shows that $r_{unstable}$ increases with increasing film thickness. For films of thickness between 7.5 ± 0.5 and 11.5 ± 0.5 nm, the experiments were more difficult to interpret. In this thickness interval, we observed an intermediate regime where isolated satellite holes appeared around a central hole or at wedge sites formed on the coalescence of neighbouring holes, but no complete cascades were seen. For films of thickness between 11 and 31 nm, the experiments did not show any satellite holes up to a central hole radius of 24 μm. From an experimental point of view, the obtainable hole radius is limited by coalescence between neighbouring holes.

So far, basic simulations performed for different film thicknesses have confirmed the general trend observed in the experiments. It should be noted that the simulation data (plotted in

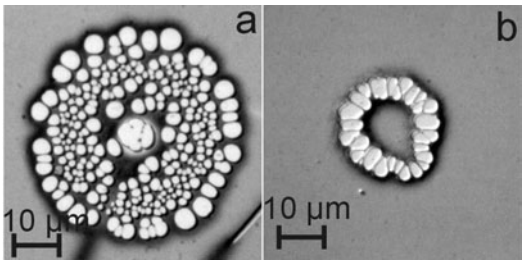

Figure 6. (a), (b) Optical micrographs of two different PS (675 k) films, of thickness 80 nm, on top of a silanized silicon wafer. Both films were annealed at 130 °C for 15 min.

figure 5 as empty triangles) refer to the distance covered by the contact line (a straight front, not a hole radius). As shown in figure 5, simulations detected the appearance of satellite holes only in films of thickness up to 11 nm and for covered distances up to about 4 μm. Films of thickness 19 nm did not show satellites holes for distances up to 12.5 μm. The results of the simulations are in turn limited by the finite size of the area used in the calculations. Further simulations on larger area will be performed in order to overcome the spatial limitation of the experiments. Slight differences between experiments and simulations are to be expected because the actual viscosity of the prepared films is known only within one order of magnitude [26] and effects due to film slippage of the polymer melt are not taken into account in the simulations. In addition, the simulations do not faithfully cover all fluctuation effects present in the experimental system. Small-scale fluctuations of the film tend to make the analysis of the experimental patterns much more involved.

The study of intentionally indented polymer films can be of great help in distinguishing hydrodynamic cascade patterns from patterns derived from random defects in the films. Examples of the latter are provided in figure 6, which shows circular patterns developed in high molecular weight PS films dewetting on silanized silicon wafers. These structures probably originated from a preexisting ring-defect on the film due to the drying of a liquid drop [37]. In figure 6(a) larger holes are situated on the outer part of the pattern rather than in the inner part, i.e. the outer holes where preexisted the inner ones (as in the ring of figure 6(b)). The satellite hole patterns studied in this work and in the work by Becker *et al* [28] show instead growth in the opposite direction, from a central hole towards the outside. Furthermore, we have shown that a wedge site is the preferential site for the appearance of a satellite hole, while no holes are observed in the wedges existing in several sites of the patterns in figures 6(a) and (b). Our study creates a clear distinction between such morphologies and true satellite hole patterns.

5. Conclusions

In this paper, we have described experiments and simulations on the decay of unstable PS films initiated by artificial indentations. The dynamics of these particular initial states gives a detailed insight into the dynamics of thin film decay that is difficult to obtain from the study of randomly decaying films. The evolution of the resulting rim and satellite holes in both experiment and simulations is strikingly similar, as demonstrated by figures 2 and 3. The timescales of experiments and simulations are of the same order of magnitude. In both cases the origin of time is chosen to be when the first satellite hole appears.

Our simulations provide an insight into the mechanism of satellite hole formation. We observe that the formation of the satellite holes originates in the depression developing on the wet side of the liquid rim. The depressions are in turn correlated with regions where the rim is thicker and/or has a higher curvature. In these regions, the generalized Laplace pressure at the kink acts as a nucleation centre for hole formation which then occurs inside the depression.

This effect is present in the linear indentation geometry and is particularly pronounced in the 'wedge' geometry, where the first hole behind the rim is nucleated at the acute intersection of the two rims. Furthermore, we can conclude that the time taken for satellite holes to appear increases with increasing film thickness. For films thicker than about 11 nm, no satellite holes could be observed either in simulations or in experiments and therefore a value for $r_{unstable}$ could not be determined. However, it is possible that in simulations this limit could be overcome if the lateral dimensions of the simulation area were increased.

Acknowledgment

This work was supported by the DFG under its priority programme 'Wetting and Structure Formation at Interfaces'.

References

[1] de Gennes P G 1985 *Rev. Mod. Phys.* **57** 827
[2] Srolovitz D J and Safran S A 1986 *J. Appl. Phys.* **60** 255
[3] Léger L and Joanny J F 1992 *Rep. Prog. Phys.* **55** 431
[4] Elbaum M and Lipson S G 1994 *Phys. Rev. Lett.* **72** 3562
[5] Herminghaus S, Jacobs K, Mecke K, Bischof J, Fery A, Ibn-Elbhaj M and Schlagowski S 1998 *Science* **282** 916
[6] Zhao W, Rafailovich M H, Sokolov J, Fetters L J, Plano R, Sanyal M K, Sinha S K and Sauer B B 1993 *Phys. Rev. Lett.* **70** 1453
[7] Xie R, Karim A, Douglas J F, Han C C and Weiss R A 1998 *Phys. Rev. Lett.* **81** 1251
[8] Herminghaus S, Fery A, Schlagowski S, Jacobs K, Seemann R, Gau H, Mönch W and Pompe T 1999 *J. Phys.: Condens. Matter* A **11** 57
[9] Kim H I, Mate C M, Hannibal K A and Perry S S 1999 *Phys. Rev. Lett.* **82** 3496
[10] Sferrazza M, Heppenstall-Butler M, Cubitt R, Bucknall D, Webster J and Jones R A L 1998 *Phys. Rev. Lett.* **81** 5173
[11] Higgins A M and Jones R A L 2000 *Nature* **404** 476
[12] Reiter G, Sharma A, Casoli A, David M-O, Khanna R and Auroy P 1999 *Langmuir* **15** 2551
[13] Reiter G 1992 *Phys. Rev. Lett.* **68** 75
[14] Blossey R 1995 *Int. J. Mod. Phys.* B **9** 3489
[15] Bischof J, Scherer D, Herminghaus S and Leiderer P 1996 *Phys. Rev. Lett.* **77** 1536
[16] Redon C, Brochard-Wyart F and Rondelez F 1991 *Phys. Rev. Lett.* **66** 715
[17] Jacobs K, Herminghaus S and Mecke K R 1998 *Langmuir* **14** 965
[18] Vrij A 1966 *Discuss. Faraday Soc.* **42** 23
[19] Brochard-Wyart F and Daillant J 1990 *Can. J. Phys.* **68** 1084
[20] Siggia E D 1979 *Phys. Rev.* A **20** 595
[21] Mitlin V S 1993 *J. Colloid Interface Sci.* **156** 491
[22] Sharma A and Khanna R 1998 *Phys. Rev. Lett.* **81** 3463
[23] Seemann R, Herminghaus S and Jacobs K 2001 *Phys. Rev. Lett.* **86** 5534
[24] Seemann R, Herminghaus S and Jacobs K 2001 *Phys. Rev. Lett.* **87** 196101
[25] Neto C, Jacobs K, Seemann R, Blossey R, Becker J and Grün G 2003 *J. Phys.: Condens. Matter* **15** S421
[26] Herminghaus S, Jacobs K and Seemann R 2001 *Eur. Phys. J.* E **5** 531
[27] Kargupta K, Konnur R and Sharma A 2001 *Langmuir* **17** 1294
[28] Becker J, Grün G, Seemann R, Mantz H, Jacobs K, Mecke K R and Blossey R 2003 *Nat. Mater.* **2** 59
[29] Sherman R, Hirt D and Vane R 1994 *J. Vac. Sci. Technol.* A **12** 1876
[30] Brandrup J and Immergut E H (ed) 1975 *Polymer Handbook* 2nd edn (New York: Wiley-Interscience)
[31] Seemann R, Herminghaus S and Jacobs K 2001 *J. Phys.: Condens. Matter* **13** 4925
[32] Grün G and Rumpf M 2000 *Numer. Math.* **87** 113
[33] Ciarlet Ph G 1978 *The Finite Element Method for Elliptic Problems* (Amsterdam: North-Holland)
[34] Grün G 2003 On the numerical simulation of wetting phenomena *Numerical Methods of Composite Materials Proc. 15th GAMM-Sem. (Kiel)* ed W Hackbusch and S Sauter (Braunschweig: Vieweg) at press
[35] Grün G 2003 *Math. Comput.* at press
[36] Herminghaus S, Seemann R and Jacobs K 2002 *Phys. Rev. Lett.* **89** 56101
[37] Deegan R D, Bakajin O, Dupont T F, Huber G, Nagel S R and Witten T A 1997 *Nature* **389** 827